Proceedings World Geothermal Congress 2015
Melbourne, Australia, 19-25 April 2015

Modeling of Propagation of Interacting Cracks Under Hydraulic Pressure Gradient

Hai Huang, Earl Mattson and Rob Podgorney

Idaho National Laboratory, PO Box 1625, MS2025, Idaho Falls, ID83415, USA

E-mail: Hai.Huang@inl.gov

Keywords: hydraulic fracturing, interacting cracks, modeling

ABSTRACT

A robust and reliable numerical model for fracture initiation and propagation, which includes the interactions among propagating fractures and the coupling between deformation, fracturing and fluid flow in fracture apertures and in the permeable rock matrix, would be an important tool for developing a better understanding of fracturing behaviors of crystalline brittle rocks driven by thermal and (or) hydraulic pressure gradients. In this paper, we present a physics-based hydraulic fracturing simulator based on coupling a quasi-static discrete element model (DEM) for deformation and fracturing with conjugate lattice network flow model for fluid flow in both fractures and porous matrix. Fracturing is represented explicitly by removing broken bonds from the network to represent microcracks. Initiation of new microfractures and growth and coalescence of the microcracks leads to the formation of macroscopic fractures when external and/or internal loads are applied. The coupled DEM-network flow model reproduces realistic growth pattern of hydraulic fractures. In particular, simulation results of perforated horizontal wellbore clearly demonstrate that elastic interactions among multiple propagating fractures, fluid viscosity, strong coupling between fluid pressure fluctuations within fractures and fracturing, and lower length scale heterogeneities, collectively lead to complicated fracturing patterns.

1. INTRODUCTION

The advancement of EGS greatly depends on our understanding of the dynamics of the strongly coupled thermo-hydro-mechanical (THM) processes and our ability to reliably predict fracturing process of low permeability crystalline rocks under stimulation and production conditions [1]. During the past a few decades, a number of hydraulic fracturing models have been developed and reported in literature, including classic Perkins–Kern–Nordgren (PKN) and Khristianovich–Geertsma–DeKler (KGD) models [2,3,4] that require assumptions such as bi-wing planar fracture growth, elliptical fracture geometry, and homogeneous rock mechanical properties. In recent years, a number of e new numerical hydraulic fracture propagation models, largely based on the variations of finite element models (FEM) such as extended FEM (XFEM) and cohesive zone FEM methods were also developed too [5-8] to handle mechanical deformations and fracture propagation, and coupled them with various continuum flow models. Many of the current hydraulic fracturing models still handle only simple fracture geometries, or require using empirical failure criteria and post-failure mechanical/hydraulic constitutive laws, and simplified fluid-solid coupling methods. Despite of that many progress have been made and important knowledge were obtained regarding to hydraulic fracturing, it still remains a challenging task for developing a reliable and robust hydraulic fracture model that appropriately account for (1) random initiation of fractures; (2) strongly nonlinear coupling among deformation, fracturing and fluid flow in fracture apertures and leakage into porous rock matrix; and (3) interactions between propagating fractures and heterogeneities at various scales, including natural fractures

In this paper, we present a physics-based rock deformation and fracture propagation simulator by using a quasi-static discrete element model (DEM) to describe the fracturing and a network flow model to simulate fluid flow in both fractures and porous rock. This paper details the methodology of the DEM for fracturing and how a network flow model is coupled with the DEM model. Numerical simulation results of the hydraulic fracturing process from a horizontal wellbore will be presented.

2. METHODOLOGY

2.1. Quasi-static discrete element model (DEM)

The discrete element model (DEM), originally introduced by *Cundall and Strack* [10] over 30 years ago, has been widely used to model the mechanical deformation and fracturing of polycrystalline rocks at various scales in geotechnical engineering community, ranging from grain-scale microcracks to large scale faults associated with earthquakes. In DEM models, illustrated by Figure 1, a volume of rock is represented by a network of nodes (also referred as particles) of variable sizes connected by elastic beams. The force and moment exerting on a node *i* by a neighboring node *j* are given by

$$\vec{F}_{i,j} = k_n(d_{i,j} - d^0_{i,j})\vec{n}_{i,j} + k_s \frac{1}{2}(\phi_{i,j} + \phi_{j,i})\vec{s}_{i,j}\,, \tag{1}$$

$$\vec{M}_{i,j} = k_s d_{i,j}[\frac{\Phi}{12}(\phi_{i,j} - \phi_{j,i}) + \frac{1}{2}(\frac{2}{3}\phi_{i,j} + \frac{1}{3}\phi_{j,i})]. \tag{2}$$

Here $d_{i,j} = \left|\vec{\mathrm{x}}_i - \vec{\mathrm{x}}_j\right|$ is the distance between the centers of two DEM nodes (the centers of the corresponding particles), *i* and *j*, and $d^0_{i,j} = r_i + r_j$ is the initial equilibrium (stress free) distance, where r_i is the radius of the i^{th} particle. $\vec{n}_{i,j}$ and $\vec{s}_{i,j}$ are the unit vectors parallel and perpendicular to the center line connecting nodes *i* and *j*, $\phi_{i,j}$ is the rotation angle in the local frame of the

beam, $\vec{t}_{i,j}$ is the unit vector parallel to the tangent of the bent beam at node *i*. k_n and k_s are the normal and shear force constants. If a regular square [11] or triangular [9] lattice is used in the simulation, k_n and k_s are related to the macroscopic Young's modulus E_0, shear modulus G_0 and Poisson's ratio ν by $k_n = E_0 A / d$, $k_s = 12E_0 I[d^2(1+\Phi)]$ and $\Phi = 12E_0 I / G_0 A d^2$, where *A* is the cross-section area of the elastic beam and *I* is the geometric part of its moment of inertia. Since a random DEM network was used in our simulations (to avoid the effects of the lattice symmetry on the fracturing pattern), k_n and k_s must be calibrated against the desired E_0 and ν. At mechanical equilibrium, the total force and moment acting on every DEM node must vanish, giving rise to the Cosserat elasticity equations in the continuum limit.

Once a mechanical load is applied (in our problem the load is imposed by the injection of fluids), an over-relaxation algorithm is used to relax the DEM network to a new state of mechanical equilibrium in which the net forces and moments are zero for all the DEM particles. If a beam satisfies the von Mises failure criterion

$$\tau = \left(\frac{\varepsilon}{\varepsilon_c}\right)^2 + \frac{\max(|\phi_{i,j}|, |\phi_{j,i}|)}{\phi_c} > 1 \,, \tag{3}$$

it is irreversibly removed from the DEM network, giving rise to crack initiation and growth. Here ε is the longitudinal strain of the beam, and ε_c is the critical longitudinal tensile strain (the maximum tensile strain that the bond can sustain), and ϕ_c is the critical rotational angle above which the bond will break, even in the absence of tensile strain. Typical values for ε_c and ϕ_c range from ~10^{-3} to ~10^{-2} for rocks and many other polycrystalline brittle solids. After a beam has broken stress is transferred throughout the system by the long range elastic interactions, but mainly to neighboring beams, and they are likely to break immediately or after a short lapse in time. A sequence of "coupled" beam breaking events mimics the fracture propagation process, and this unique feature makes DEM models a powerful method for studying the random initiation and subsequent propagation of cracks.

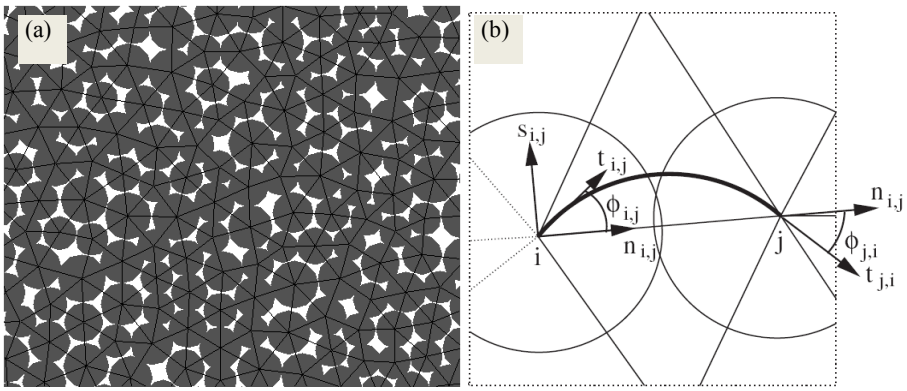

Figure 1. Illustration of a 2-dimensional (2D) DEM model: (a) a discrete element network generated by random packing of particles of variable sizes with a uniform size distribution; and (b) a bent elastic beam connecting nodes *i* and *j* used for DEM model (modified from [9])

2.2. Conjugate network flow model

The governing equation for fluid flow is taking the following form

$$\frac{\partial(n\rho_f)}{\partial t} = \nabla\left(\frac{\rho k_0}{\mu}\nabla P\right) + \rho_f Q, \tag{4}$$

where *n* is the porosity of porous medium, ρ_f is the density of fluid, k_0 is the formation permeability, μ is the fluid viscosity, *P* is fluid pressure, and *Q* is the volumetric injection rate. Using the definitions for fluid compressibility $c_f = \frac{1}{\rho_f}\frac{\partial \rho_f}{\partial P}$ and rock matrix bulk compressibility (inverse of bulk modulus) $c_n = \frac{1}{n}\frac{\partial n}{\partial P}$, the term on the left hand of eq. (4) can be rewritten as

$$\frac{\partial(n\rho_f)}{\partial t} = \left(\rho_f n c_f + \rho_f n c_n\right)\frac{\partial P}{\partial t}. \tag{5}$$

Substituting eq. (5) into eq. (4), defining total compressibility $c_T = c_f + c_n$, and then rearranging terms, we obtain

$$\frac{\partial(nP)}{\partial t}=\nabla\left(\frac{k_0}{c_T\mu}\nabla P\right)+\frac{Q}{c_T}. \tag{6}$$

By choosing a characteristic length L^* and a characteristic time t^*, eq. (6) can be rewritten in a dimensionless form

$$\frac{\partial(nP)}{\partial t'}=\nabla'\left(\frac{k_0}{c_T\mu}\frac{t^*}{L^{*2}}\nabla' P\right)+\frac{Qt^*}{c_T}=\nabla'\left(\lambda\nabla' P\right)+\frac{Qt^*}{c_T}. \tag{7}$$

By further normalizing the fluid pressure P by Young's modulus E and dropping the prime sign in eq. (7), we finally reach a dimensionless fluid pressure diffusion equation

$$\frac{\partial(np)}{\partial t}=\nabla(\lambda\nabla p)+Q^*, \tag{8}$$

with dimensionless pressure $p=P/E$, dimensionless injection rate $Q^*=Qt^*/(c_TE)$ and dimensionless pressure diffusivity $\lambda=k_0t^*/c_T\mu L^{*2}$.

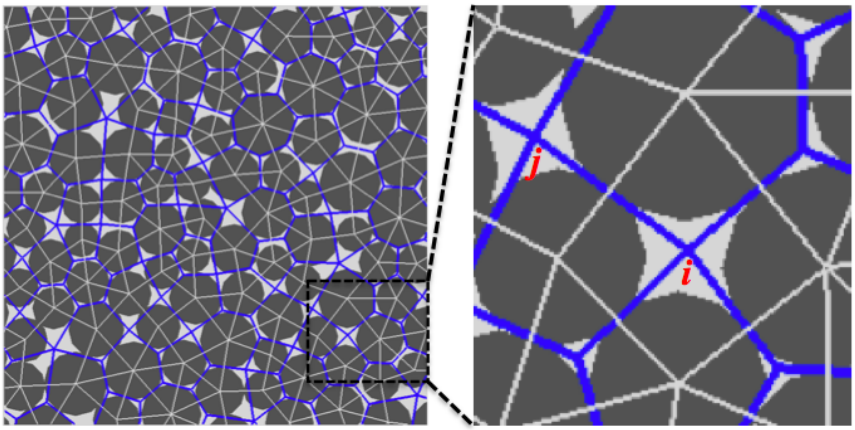

Figure 2. The concept of conjugate lattice (blue lattice) for network flow modeling and coupling with the DEM network (white lattice).

As illustrated in Figure 2, a network flow model using a lattice conjugate to the DEM lattice is used to discretize eq. (8) by a finite volume scheme:

$$\Delta V_i n_n\frac{p_i^{t+\Delta t}-p_i^t}{\Delta t}=\sum_{j=1}^{neighbor}\lambda_{ij}A_{ij}\frac{p_j^{t+\Delta t}-p_i^{t+\Delta t}}{d_{ij}}+Q^*\Delta V_i, \tag{9}$$

where ΔV_i is the control volume associated with flow node i, d_{ij} is the distance between nodes i and j, A_{ij} is the cross section area between nodes i and j. The discretized equations are solved by a multigrid solver.

The fluid pressure gradient exerts forces on individual elements of the discrete element network through the following form:

$$\vec{F}_{i,j}=k_n(d_{i,j}-d_{i,j}^0)+k_s\frac{1}{2}(\varphi_{i,j}+\varphi_{j,i})\vec{s}_{i,j}-\nabla P\cdot\pi r_i^2, \tag{10}$$

$$\vec{M}_{i,j}=k_s d[\frac{\Phi}{12}(\varphi_{i,j}-\varphi_{j,i})+\frac{1}{2}(\frac{2}{3}\varphi_{i,j}+\frac{1}{3}\varphi_{j,i})], \tag{11}$$

where ∇P is the fluid pressure gradient acting on individual DEM particle, which can be obtained from the nodal pressure values on its neighbor conjugate flow lattice. As fluid pressure (and pressure gradient) increases due to fluid injection during hydraulic stimulation, the force exerted on the DEM particles also increases and deforms the mechanical bonds and breaks them if the deformation reaches a prescribed threshold value, thereby initiating fracturing. As shown in Figure 2, each mechanical bond intersects with the flow network. When a mechanical bond is broken, a microfracture perpendicular to the bond initiates and connects the two associated fluid nodes of the flow network with a new permeability in the form

$$k=b^2/12 \tag{12}$$

Here b is the aperture of the microfracture (same as the separation distance of the two neighbor DEM particles subject to fracturing). The new permeability is then used to recalculate the hydraulic diffusivity λ_{ij} in eq. (9).

The simulation of coupled DEM-network flow model consists of interleaved fluid flow, mechanical relaxation of the DEM network and beam breaking steps. During each time step, the new fluid pressure field (in both fractures and matrix) is obtained first by

solving eq (9). Then the new fluid pressure field is applied to DEM network according eqs. 10-11, and the DEM network is relaxed to a new mechanical equilibrium. The beam that most exceeds the failure criteria, which is usually near a crack tip, is then removed from the DEM network and the network is again relaxed into a new state of mechanical equilibrium. The mechanical relaxation and beam breaking are repeated a number of times during each time step, mimicking crack initiation and propagation, until no additional beam-breaking occurs, and the simulation then proceeds to a new time step. This quasi-static approach to modeling hydraulic fracturing is reasonable, since stress build up and relax associated with hydraulic fracture propagations often exhibit quasi-static behaviors.

It is also worth noting that our coupled DEM-network flow model accounts for both flow in fractures and flow into the rock matrix, unlike most other network flow models that typically only account for fluid flow in fractures. This unique feature allows our model to evaluate the leakage of fracturing fluid into the porous matrix.

3. DEM MODEL CALIBRATION

The DEM model parameters k_n, k_s, ε_c and ϕ_c must be calibrated to accurately represent the mechanical properties of brittle rocks such as the Young's modulus E_0, Poisson's ratio ν, tensile strength σ_t and compressive strength σ_c. The calibration of DEM model parameters was performed by simulating uniaxial tensile/compression tests as shown in Figure 3. For this purpose a model domain of size 50 x 100 (dimensionless) was discretized by using a random packing algorithm with 6,143 DEM nodes (circular discs) of variable radii selected from a uniform random distribution with an average radius of 0.5 and maximum to minimum radius ratio of 2. The dimensionless force constants k_n were selected randomly from a Gaussian distribution with a mean of μ = 1.0 and a standard deviation of σ = 0.1. A constant k_s / k_n ratio of 0.2 was used in all simulations. k_n and k_s / k_n jointly determine the macroscopic Young's modulus E_0 and Poisson's ratio ν. The critical tensile strains ε_c of the beams were selected randomly from a Gaussian distribution with a mean of μ = 0.3% and a standard deviation of σ = 0.03%. The critical rotation angles ϕ_c were also selected from a Gaussian distribution with μ = 0.5% and σ = 0.05%. The beam failure parameters ε_c and ϕ_c jointly determine the macroscopic tensile and compressive strength of the rock. During the numerical uniaxial tension (or compression) test, DEM particles near both ends move uniformly in opposite directions at a specified strain rate in order to mimic uniaxial tensile (or compressive) loading condition. At each loading stage, the averaged axial stress and lateral strain within the sample were calculated by volume averaging in order to generate stress-strain curves. Figures 3a and 3b show the vertical stress fields prior to macroscopic failure under tensile and compressive loads. On average, the stress field is homogeneous, only in a statistical sense. The stress varies locally, which plays an important role in the random nucleation of microcracks. Figures 3c and 3d show the vertical stress fields as well as macroscopic failure patterns under tensile and compressive loads. As shown in Figure 3c, an irregular macroscopic tensile crack that fluctuates about the direction perpendicular to tensile loading direction was formed. Compressive loading generates much more complex fracture patterns, as shown in Figure 3d, but the development of major shear planes due to the compressive load can be clearly seen. The sample failed (in a macroscopic sense) by shear, which is often observed in laboratory core tests.

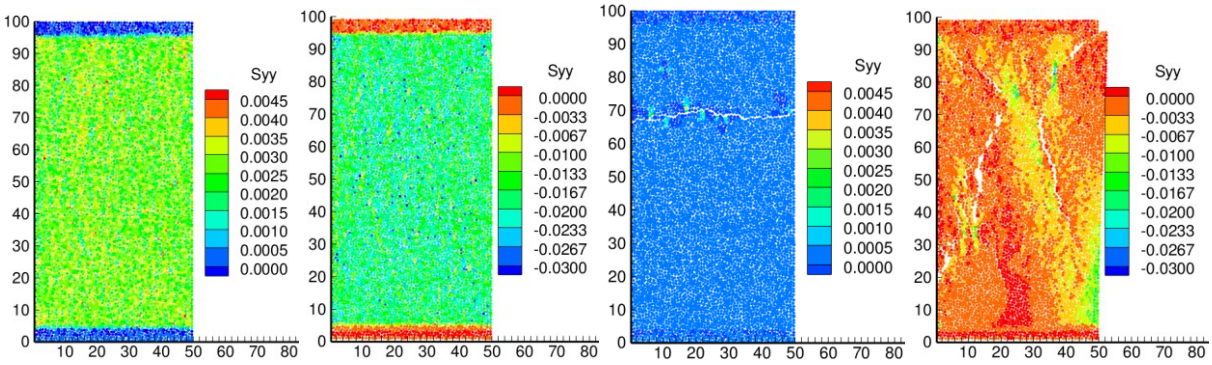

Figure 3. DEM Model calibration through numerical uniaxial tension and compression test: (a) vertical stress (dimensionless) distribution prior to tensile failure of the sample; (b) the vertical stress field (dimensionless) prior to compressive failure of the sample; (c) vertical stress (dimensionless) distribution right after the tensile failure of the sample; and (d) the vertical stress field (dimensionless) right after the compressive failure of the sample.

Figure 4 shows the simulated stress-strain curves for both the tensile (Figure 4a) and compressive tests (Figure 4b). The simulated rock sample behaved like a linear elastic solid before the loads reached their peak failure values, corresponding to the linear parts of the stress-strain curves shown in figures 4a and 4b. When the loads reached their peak (failure) values, the sample failed suddenly and stresses were released rapidly. This behavior is typical for brittle rocks. Both stress-strain curves give the same (dimensionless) Young's modulus (average slopes of the linear parts of the curves) of $E = 1.6$, and Poisson ratio of $\nu = 0.25$ (determined from the ratio between lateral strain and axial strain, not shown here). The simulated sample has a macroscopic critical tensile strain of 0.175% and critical compressive strain of 1.4%, which are in the range of many polycrystalline brittle rocks. The corresponding peak tensile strength σ_t and compressive strength σ_c are 2.74e-3 and 2.20e-2, respectively. These dimensionless critical tensile and compressive stresses can then be rescaled to the dimensional macroscopic, measurable, critical tensile strength of the rock (by multiplying with $E_0 / 1.6$).

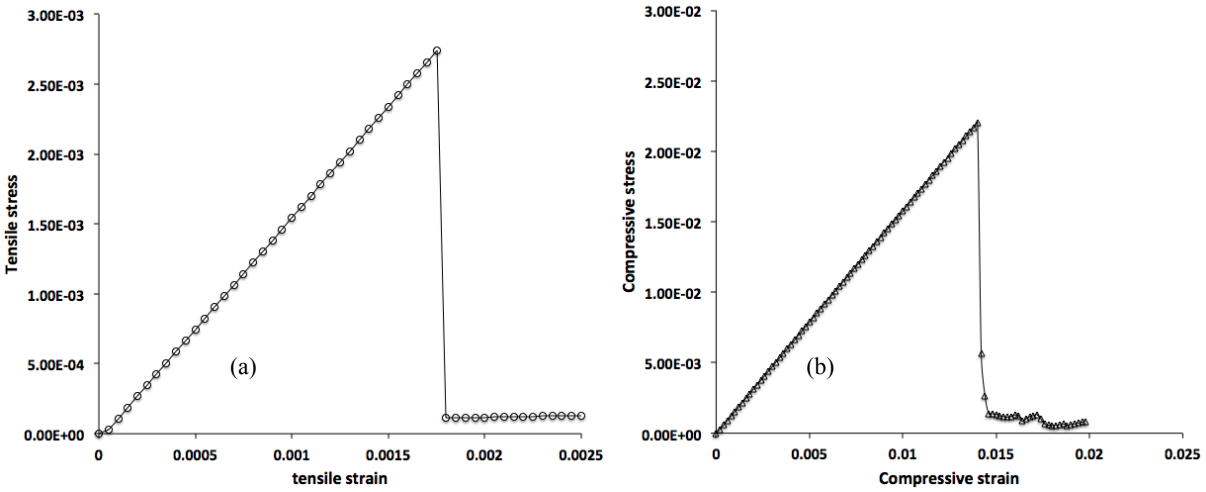

Figure 4. Simulated stress-strain curves for the calibration tests: (a) uniaxial tension and (b) uniaxial compression tests.

By broadening the random distributions for k_n and ε_c, the DEM model can produce ductile behavior. However, issues such as the effects of particle size distribution and the widths of the distributions of the mechanical properties of the beams are beyond the scope of this study and information about such issues can be found in [12] and references therein. The calibration results shown in figures 3 and 4 clearly demonstrate the unique strength of the DEM model for simulating the random initiation, propagation and coalescence of microcracks, and eventual macroscopic failure. This modeling approach allows cracking processes to be investigated in a systematic manner, which would be difficult or impossible to do experimentally because of sample-to-sample variability and challenge of preparing a series of materials with different, but accurately known mechanical properties under a wide range of well-controlled conditions.

4. NUMERICAL RESULTS

Here we present a few two-dimensional hydraulic fracturing simulation examples to illustrate the strength of the coupled DEM-network flow model to capture important physics and the effects of injection rates, fluid viscosity and heterogeneity on fracturing patterns.

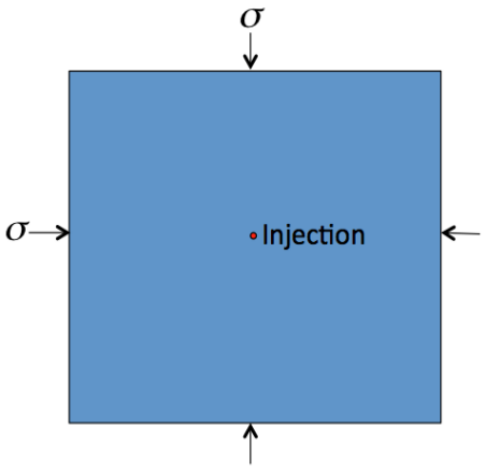

Figure 5. Model setup for single well injection with hydrostatic confining stress state

4.1 Hydraulic fracturing from a vertical well

As shown in Figure 5, an injection well is placed at the center of the model domain. In the simulation, a fluid node on the flow network located in the center of the domain is chosen to be the injection source. The matrix has a dimensionless hydraulic pressure diffusivity λ of ~10^{-8}, corresponding to tight formations with extremely low permeability on the order of 10^{-19} m^2 and high-viscosity fracking fluid with viscosity of ~10^{-2}*Pa.s*, about 10-100 times greater than that of clean water. A hydrostatic stress state is considered in this example.

Figure 6 shows the simulated fracture propagation patterns at two different injection rates. As shown in Figure 6a, under hydrostatic confinement condition and higher injection rate, fracture growth appears to have a dendrite-type growth pattern, branching along the previous generated fractures in a random way, a geometric property that is typically observed for self-similar (fractal) structures. The simulated fracture growth pattern is very similar to experimental observations using Hele-Shaw cells and other laboratory fracturing experiments. Branching of fractures is resulted from a complex interplay between the fluid pressure losses along fractures due to viscous friction and the growth of fractures. It is interesting to note that branching always occur somewhere

along previous fractures and behind their tips. At smaller injection rate (in this example, the injection rate is reduced by a factor of 2), as shown in Figure 6b, multiple fractures can still be initiated around the injection wellbore and continue to grow for a long distance without branching (we expect branching will eventually occur as long as the domain is larger and injection continues, but at later time). This is due to the fact that at smaller injection rate, fluid velocity in fractures is smaller, thus leading to smaller pressure drop from the wellbore to crack tips. Therefore sufficient stress is transmitted to near the crack tips allowing those cracks to continuously grow.

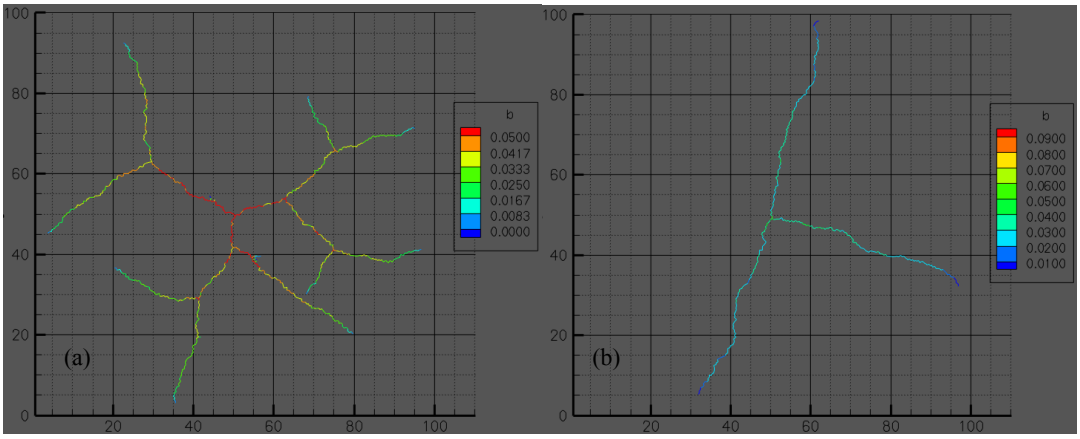

Figure 6. Comparison of simulated fracturing patterns using two different injection rates: (a) high injection rate and (b) small injection rate. Fractures are colored by their apertures (dimensionless).

Also as shown in Figure 6, the crack apertures closer to the injection well are generally the largest and decrease with the distance from the injection well. It's also obvious in the simulation results that higher injection rate leads to larger apertures on average than does small injection rate, which is not surprising and consistent with laboratory and field observations.

Fluid viscosity is an important parameter in hydraulic fracturing. Therefore, we performed another simulation under the same conditions as those shown in Figure 6a, but with a much smaller fluid viscosity, ~100 times smaller than that used in previous example (comparable to the viscosity of water). This is done conveniently by simply increase the dimensionless hydraulic diffusivity λ. Figure 7 shows the comparison of the simulated fracturing patterns.

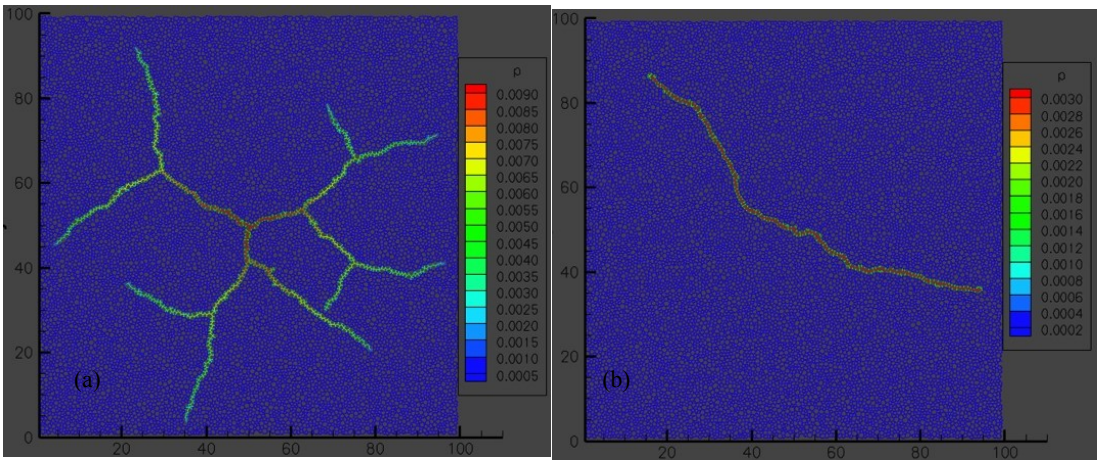

Figure 7. Comparison of fracturing patterns using fracking fluid of different viscosities: (a) high viscosity and (b) low viscosity. Color scales with the fluid dimensionless fluid pressure (normalized by Young's modulus).

It is obvious that high viscosity fluid leads to dendrite-type fracturing patterns involving branching at different stages due to the larger fluid pressure loss from the wellbore to fracture tips. However, when fluid viscosity is small, as shown in Figure 7b the fluid pressure loss is small along newly opened fracture, which keeps driving the newly opened fracture continuously propagating into a greater distance, resulting in much less number of fractures: often a single long discrete fracture. This might have negative impact to the recovery rate.

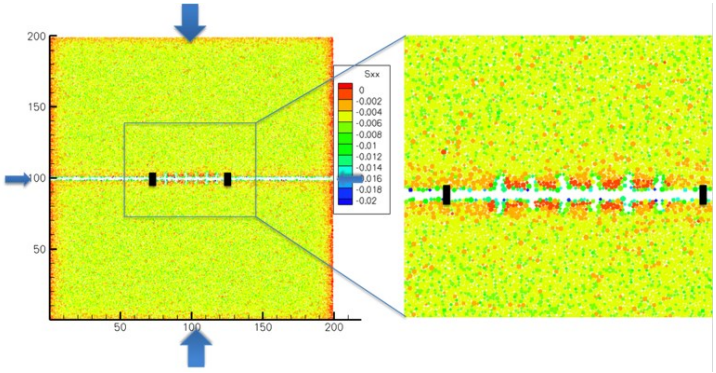

Figure 8. (left) Model set up for a multi-stage horizontal wellbore with maximum compressive stress in vertical direction and minimum compressive stress in horizontal direction and (right) the details of perforations. Assuming symmetry condition on either side of the wellbore, the actual simulations are only using the upper half of the conceptual model domain.

4.2 Hydraulic fracturing from a perforated horizontal wellbore

The calibrated DEM model was then used simulate propagations of hydraulic fractures from a perforated horizontal wellbore. Figure 8 shows the model setup. The matrix has a dimensionless hydraulic pressure diffusivity λ of ~10^{-10}, corresponding to tight formations with extremely low permeability on the order of 10^{-19} m^2 and fracking fluid with viscosity of $0.8 Pa.s$, about ~1000 times greater than that of clean water. Fracking fluid is injected at constant rate into one stage (plugged on both ends) of a horizontal wellbore, which has initial 6 perforations. It is worthy noting that these initial perforations have some random perturbations in their sizes and depths into the formation, which come out naturally from our DEM model as a result of a random packing procedure used to construct the model. The maximum confining compressive stress applied to the model corresponds to a value of ~80MPa (~11,000psi) along the vertical direction, with a maximum to minimum (horizontal) ratio of 2.

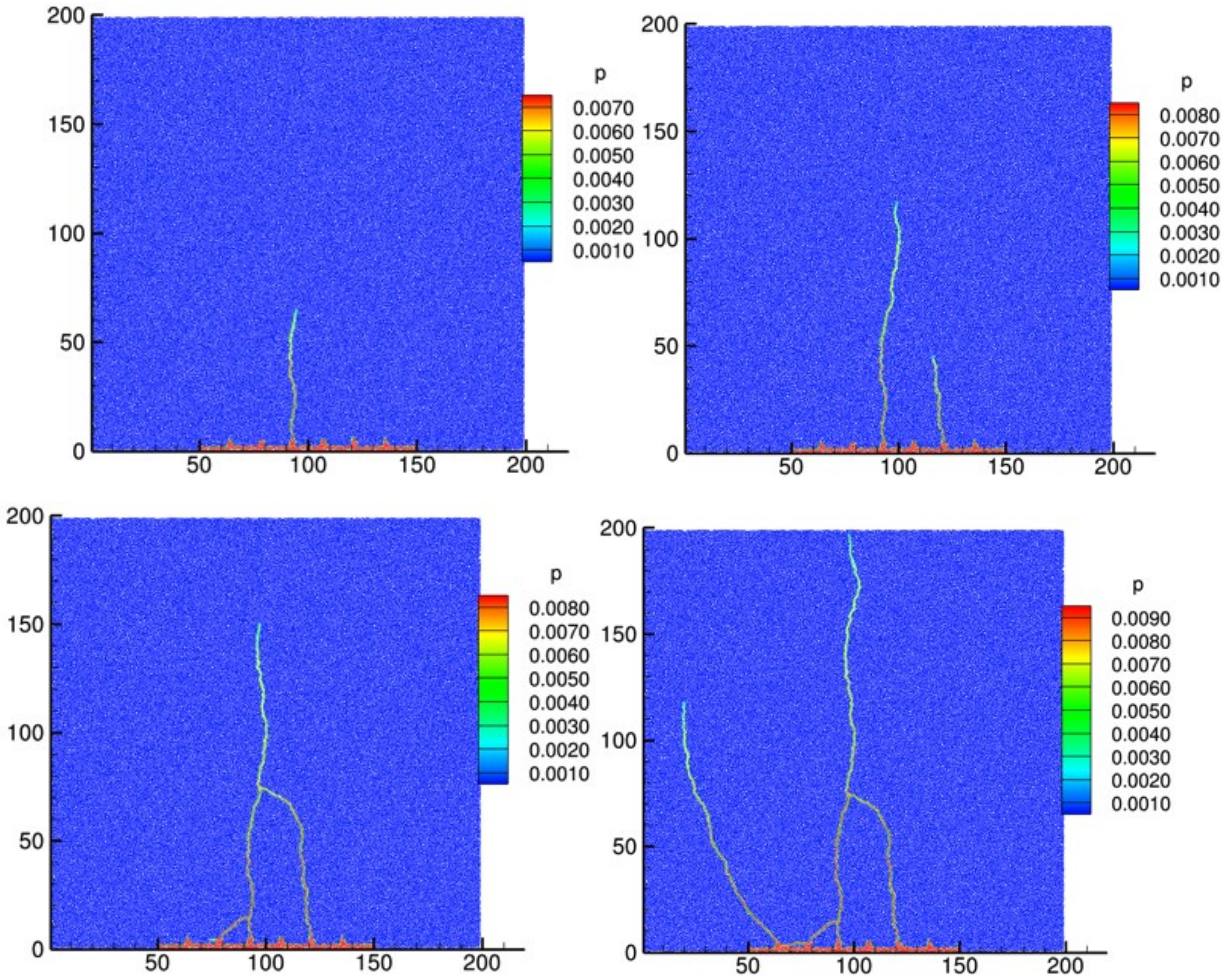

Figure 9. The simulated fracture propagation process from a horizontal wellbore with multiple perforations using high viscosity fluid. Color scales with fluid pressure (dimensionless).

Figure 9 shows the snapshots of the fracture propagation process. A single crack is initiated first and starts to propagate into a certain distance (Figure 9a). However, the fluid pressure loss along the fracture is significant due to high fluid viscosity. Therefore,

as the crack length increases, the growth speed also slows down, thus the wellbore pressure continues to build up, a second crack then starts to initiate and propagate simultaneously along with the previous crack, as shown in Figure 9b. As the two cracks continue to grow simultaneously, the shorter crack turns toward the longer crack (Figure 9c), and eventually terminates, while the longer crack continues to grow. It is at this stage, a third crack from another perforation starts to grow too, but quickly turns and terminates at previous crack. As injection continues (Figure 9d), another new crack is initiated and grow simultaneously with the previously formed longer crack, but at a faster speed primarily due to its shorter length that leads to smaller fluid pressure loss along that crack. It is obvious that under the same conditions, the higher viscosity fluid leads too much more complicated fracturing patters than the low viscosity fluid does.

5. CONCLUSIVE REMARKS

The simulation results of hydraulic fracture propagation and growth patterns clearly demonstrate the strength of the coupled DEM-network flow modeling approach, which could lead towards better understanding of the complex behaviors of coupled flow and fracturing processes during hydraulic stimulation of reservoirs. While the behavior of two-dimensional and three-dimensional systems are quantitatively different, two dimensional simulations like in this study provide valuable insights into this complex, coupled flow-fracturing problem.

The simulated crack patterns are drastically different from the idealized fracture patterns that typically assume more-or-less parallel, straight cracks propagating nearly uniformly from all perforations, or bi-wing straight crack. In general, the complicate fracturing patterns observed in our simulations (which are very likely to be the case in the field) can be explained by two types of interactions among cracks: (1) crack-crack interaction through elastic stress/strain field, a stress shadow concept and (2) crack-crack interaction through fluid pressure variations and dissipation in fracture networks. While the first type of crack-crack interaction has been known for a long time and studied extensively, the second type of crack-crack interaction is less well understood. In low and ultralow permeability formations, the fluid pressure variations in one crack can be rapidly diffused back to the wellbore, thus propagate into all other cracks, which in turn will change the stress concentrations at the tips of all other cracks and affect propagations of all fractures. These interactions require the hydraulic fracturing models to account for these effects in order to make meaningful predictions.

REFERENCES

1. Massachusetts Institute of Technology, (2006). *The Future of Geothermal Energy: The Impact of Enhanced Geothermal Systems (EGS) on the United States in the 21st Century*.
2. Perkins TK, Kern LR. 1961. Widths of hydraulic fractures. *Journal of Petroleum Technology*. 13:937–949.
3. Geertsma J, de Klerk F. 1969. A rapid method of predicting width and extent of hydraulically induced fractures. *Journal of Petroleum Technology*. 21:1571–1581.
4. Nordgren RP. 1972. Propagation of a vertical hydraulic fracture. *Society of Petroleum Engineers Journal.* 12:306–314.
5. Lecampion, B. 2009. An extended finite element method for hydraulic fracture problems. *Commun. Numer. Methods Eng.*, 25(2), 121–133.
6. Dahi-Taleghani, A., and Olson, J. E. 2009. Numerical modeling of multistranded hydraulic fracture propagation: Accounting for the interaction between induced and natural fractures. *Proc., SPEAnnual TechnicalConf. and Exhibition, Society of PetroleumEngineers,* Richardson,TX, 575–581.
7. Sarris, E., and Papanastasiou, P. 2012. Modelling of hydraulic fracturing in a poroelastic cohesive formation. *Int. J. Geomech*., 12(2), 160–167.
8. Zhang, Z., and Ghassemi, A. 2011. Simulation of hydraulic fracture propagation near a natural fracture using virtual multidimensional internal bonds. *Int. J. Numer. Anal. Methods Geomech.*, 35(4), 480–495.
9. Malthe-Sorenssen, A., B. Jamtveit, and P. Meakin. 2006. Fracture patterns generated by diffusion controlled volume changing reactions, *Physical Review Letters*, 96(24).
10. Cundall, P.A. and O.D.L. Strack. 1979. Discrete numerical-model for granular assemblies. *Geotechnique*. 29(1): p. 47-65.
11. Herrmann, H. J., A. Hansen, and S. Roux. 1989. Fracture of disordered, elastic lattices in 2 dimensions, *Physical Review B*, 39(1), 637-648.
12. Potyondy, D.O. and P.A. Cundall. 2004. A bonded-particle model for rock. *International Journal of Rock Mechanics and Mining Sciences.* 41(8): p. 1329-1364.